Spectral mixing of rhythmic neuronal signals in sensory cortex

Kurt F. Ahrens[†], **Herbert Levine**[†‡], **Harry Suhl**[†], **and David Kleinfeld**[†‡§¶]

[†]Department of Physics, [‡]Center for Theoretical Biological Physics, and [§]Neurosciences Graduate Program, University of California at San Diego, La Jolla, CA 92093

Contributed by Harry Suhl, September 10, 2002

The ability to compute the difference between two frequencies depends on a nonlinear operation that mixes two periodic signals. Behavioral and psychophysical evidence suggest that such mixing is likely to occur in the mammalian nervous system as a means to compare two rhythmic sensory signals, such as occurs in human audition, and as a means to lock an intrinsic rhythm to a sensory input. However, a neurological substrate for mixing has not been identified. Here we address the issue of nonlinear mixing of neuronal activity in the vibrissa primary sensory cortex of rat, a region that receives intrinsic as well as sensory-driven rhythmic input during natural whisking. In our preparation, the intrinsic signal originates from cortical oscillations that were induced by anesthetics, and the extrinsic input is introduced by periodic stimulation of vibrissae. We observed that the local extracellular current in vibrissa primary sensory cortex contained oscillatory components at the sum and difference of the intrinsic and extrinsic frequencies. In complementary experiments, we observed that the simultaneous stimulation of contralateral and ipsilateral vibrissae at different frequencies also led to current flow at the sum and difference frequencies. We show theoretically that the relative amplitudes of the observed mixture terms can be accounted for by a threshold nonlinearity in the input–output relation of the underlying neurons. In general, our results provide a neurological substrate for the modulation and demodulation of rhythmic neuronal signals for sensory coding and feedback stabilization of motor output.

Spectral mixing provides a means to compute the sums and differences of the frequency content in two signals. This can be seen easily when mixing is accomplished by the multiplication of two sinusoids, i.e., $\cos[2\pi f_a t] \times \cos[2\pi f_b t] = \frac{1}{2}\cos[2\pi(f_a + f_b)t] + \frac{1}{2}\cos[2\pi(f_a - f_b)t]$. With the addition of low-pass filtering to isolate the difference term, spectral mixing provides a means to directly compare even small differences in the frequency content between two sensory signals (Fig. 1). This phenomenon is commonly witnessed in audition, where human subjects are sensitive to the beat, or difference frequency, between two pure tones that are played simultaneously, one in each ear (1, 2). A similar computation is required in electrolocation, where animals apparently sense the difference in frequency between their own electrical discharge and that of a neighboring fish (3), and echolocation, where the relative speed of flight between a bat and its prey is encoded in the difference in frequency between outgoing and reflected acoustic waves (4). From the perspective of motor control, the ability to compute the difference in frequency between a desired and actual frequency provides a means to compute a feedback signal to stabilize the output.

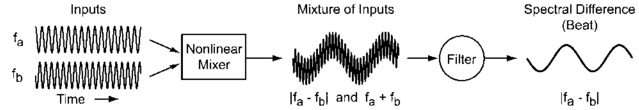

Fig. 1. Schematic of spectral mixing to compute the difference in frequency between two sinusoidal inputs. In this example the difference in frequency is small, i.e., $|f_a - f_b| \ll f_a + f_b$. The nonlinear mixing transforms the two input sinusoids into two different sinusoids with spectral components at $|f_a - f_b|$ and $f_a + f_b$. The low-pass filter removes the higher frequency component to leave only the difference term.

Here we search for an electrophysiological basis for the spectral mixing of two rhythmic signals in vibrissa primary sensory (S1) cortex of rat. Past work has shown that a subset of units in S1 cortex (5, 6) as well as units in primary motor cortex (7) form internal reference signals of vibrissa position during rhythmic whisking. The synthesis and stabilization of these references may be achieved by the neurological implementation of a phase-locked loop (7–10), a circuit that figures prominently in the feedback control of rhythmic systems (11). At the heart of a phase-locked loop is a mixer, a circuit element that computes the sums and differences in frequency between the internal reference and an external rhythmic drive (Fig. 1). We considered two paradigms to reveal such a circuit: spectral mixing (*i*) between an intrinsic oscillation induced by anesthesia and a rhythmic cortical response evoked by stimulation of the contralateral vibrissae and (*ii*) between two evoked cortical rhythms, one in response to stimulation of the contralateral vibrissae and the other in response to stimulation of the ipsilateral vibrissae at a different frequency. In either paradigm, the signature of mixing is the presence of spectral components at the sum and difference frequencies of the two fundamental frequencies in the measured signal.

Experimental Methods

Our subjects were 17 Long Evans female rats, 200–350 g in mass. One group of animals was implanted with electrodes for chronic studies such that we could record across multiple days. A second set was prepared solely for acute measurements. All recordings were with animals anesthetized through intramuscular injections of ketamine (50 mg/kg rat) and xylazine (10 mg/kg rat); atropine was administered subcutaneously (0.05 mg/kg rat). Supplemental doses of ketamine, typically 30% of initial dose, were administered to maintain inhibition of pedal and corneal reflexes. The care and experimental manipulation of our animals were in strict accord with guidelines from the National Institutes of Health (12) and have been reviewed and approved by the Institutional Animal Care Committee at University of California at San Diego.

Surgical Procedures. Animals used for chronic measurements were anesthetized with 2% halothane in humidified O_2 and secured in a stereotaxic holder. Temperature was maintained at 37°C throughout surgery and recovery. A single midline incision was made, tissue was reflected from the skull dorsum and the dorsal region of the temporal bones, and a rectangular window that extended from 2 to 4 mm posterior to Bregma and from 4 to 6 mm lateral to the midline was opened. A fine incision to the dura mater was made with the tip of a 30-gauge hypodermic needle and a silicon-based multielectrode probe (5mm100, Center for Neural Communication Technology, University of Michigan, Ann Arbor) was placed in the

---

Abbreviations: S1, vibrissa primary sensory; CSD, current source density; LFP, local field potential.

[¶]To whom correspondence should be addressed at: Department of Physics 0319, University of California, 9500 Gilman Drive, La Jolla, CA 92093. E-mail: dk@physics.ucsd.edu.

www.pnas.org/cgi/doi/10.1073/pnas.222547199

center of the incision and lowered radially with a piezoelectric drive (IW-700, Burleigh Instruments, Fishers, NY). The probe was cemented to no. 000-90 screws placed in the skull. Teflon-coated silver wires were attached to ground and reference points. The 18 wires from the probe (16 channels plus reference and ground) were brought to a connector (A7518-002, Omnetics Connector, Minneapolis, MN).

Animals used for acute studies were sedated initially with 2% halothane in humidified O_2 followed by intramuscular injection of ketamine and xylazine (see above). The remaining surgical procedure proceeded as described above except that the silicon-based probe inserted into cortex was not fixed to the skull.

Stimulation. Separate columns of vibrissae including rows B–E were captured in a fine mesh and stimulated with a piezoelectric drive of local design (13, 14). This method allows isolation of the stimulation to one side of the face. The maximum amplitude of the deflection was typically ±1°, and the pulse width was 5 ms. Pulsatile stimulation is far more effective in eliciting a cortical response than sinusoidal stimulation (15), although pulsatile stimulation explicitly evokes harmonics of the stimulation frequency.

Recordings. Potentials throughout the depth of S1 cortex were obtained simultaneously with a silicon-based, in-line radial array of 16 electrode contacts (13 by 13 μm) separated by 100 μm and plated with iridium. The iridium surfaces were prepared and tested as described (16). The signal from each electrode as well as a reference signal from an unrelated region of cortex were impedance-buffered with *n*-channel field-effect transistors (SST4118, Vishay Siliconix, Santa Clara, CA) in a common-source configuration that was placed in the complementary connector (A7640-001, Omnetics Connector). The buffered signals were differentially amplified, bandpass-filtered (0.3 Hz single-pole high pass and 75 Hz six-pole Bessel low pass; TETMD A110-2, Teledyne Electronic Technologies, Los Angeles), and digitized at $F_s = 500$ Hz.

The voltage signals measured along each silicon-based array, denoted $V(z, t)$ where z is the depth along the radial axis, were used to calculate the discrete second spatial derivative of the potential with respect to depth. The derived signal, $-\partial^2 V(z, t)/\partial z^2$, is the negative of the z component of the Laplacian of the local field potential (LFP) and is referred to as the current source density (CSD) (17). It is estimated as CSD $\cong -[V(z + \Delta z, t) - 2V(z, t) + V(z - \Delta z, t)]/\Delta z^2$, where $\Delta z = 100$ μm. A negative sign of the CSD corresponds to the flow of negative charge into a region such that the density of positive charge decreases with time. This is denoted as a current sink and may be interpreted as net depolarization of the underlying cells by local excitatory synaptic inputs. Conversely, a positive sign of the CSD corresponds to the flow of positive charge into a region and is denoted as a current source. The interpretation of this measure rests on two assumptions: (*i*) the dominant current flow is along a radial axis through cortex, consistent with the radial orientation of neurons in cortex, and (*ii*) the conductivity of cortex, on the 100-μm scale of our measurements, varies only weakly in value.

Histology. At the termination of experiments, the rats were killed by lethal overdose of nembutal (125 mg/kg rat). They were fixed by transcardial perfusion of buffered saline followed by 4% paraformaldehyde in buffered saline. The brain then was removed, equilibrated in a 30% (wt/vol) sucrose solution, frozen, sectioned with a sliding microtome at 30-μm thickness, mounted, and stained with thionin. Silicon probe tracks were identified under microscopic examination (Fig. 2*a*), and the depth of the probe in cortex was estimated from the track.

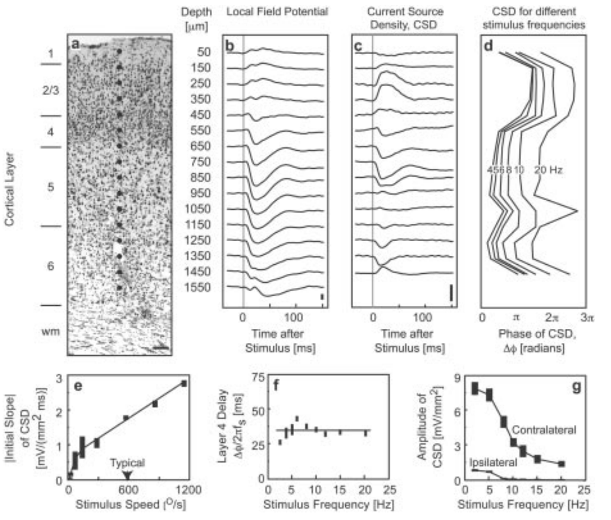

Fig. 2. Form and frequency dependence of the CSD signals in the anesthetized rat. (*a*) Photomicrograph of a 30-μm-thick coronal section of S1 cortex stained with thionin that was penetrated by the 16-channel probe. A lesion caused by the probe is seen at a depth of 1,300 μm below the pia. The labeling on the left corresponds to the approximate layer in cortex, i.e., 1–6 and the white matter (wm). (Scale bar, 100 μm.) (*b*) The LFPs simultaneously recorded at different depths below the pial surface in response to periodic taps to the vibrissa at a repetition rate of $f_{\mathrm{stim}} = 6$ Hz. The data are the average of 30 cycles. (Scale bar, 100 μV.) (*c*) The CSD derived from the LFP data in *b*. (Scale bar, 5 mV/mm².) (*d*) The phase shift of the fundamental component of CSD signal relative to the stimulus as a function of both depth below the pial surface and stimulation frequency. The phase is found from the value of the spectral coherence ($\Delta f = 0.5$ Hz with $K = 3$ and $T = 4.1$ s) evaluated at the stimulation frequency. (*e*) The magnitude of the CSD response, reported as the initial slope of the CSD response of the sink at layer 4 as a function of the angular speed of the stimulus. The bars are the SEM, and the line is drawn solely as a guide. (*f*) The time delay of the CSD response of the sink at layer 4 as a function of the stimulus repetition frequency. The straight line is drawn solely as a guide. (*g*) The difference between the maximum and minimum value of the CSD response at layer 4 as a function of the stimulus repetition frequency.

Spectral Analysis. Spectra power densities of individual time series of CSD activity, denoted $\mathbf{S}(f)$ below, were calculated with the direct multitaper spectral estimation techniques of Thomson (18); this procedure minimizes the leakage between neighboring frequency bands. In brief, the spectral power is defined in terms of an average over all instances and tapers, i.e.,

$$\mathbf{S}(f) \equiv \frac{1}{NK}\sum_{n=1}^{N}\sum_{k=1}^{K}\tilde{\mathbf{V}}^{(n,k)}\tilde{\mathbf{V}}^{*(n,k)}, \qquad [1]$$

where

$$\tilde{\mathbf{V}}^{(n,k)} \equiv \{\tilde{\mathrm{V}}^{(n,k)}(f)\}_{f=0}^{F_s/2} = \frac{1}{F_s}\sum_{t=0}^{T} e^{i2\pi ft}\mathrm{V}^{(n)}(t)w^{(k)}(t) \qquad [2]$$

is the discrete Fourier transform of the product of the measured time series $\mathbf{V}^{(n)} \equiv \{\tilde{\mathrm{V}}^{(n)}(t)\}_{t=0}^{T}$, with the kth Sleppian taper, $\mathbf{w}^{(k)} \equiv \{\mathrm{w}^{(k)}(t)\}_{t=0}^{T}$. Numerically, $\tilde{\mathbf{V}}^{(n,k)}$ is computed as the fast Fourier transform of the product after it is padded to at least four times the initial length. The parameter T is duration of the data trace, N is the number of instances of the waveform, and K is the number of tapers in a given spectral estimate such that NK is the total number of degrees of freedom. In this procedure, the spectrum is averaged over a half-bandwidth of

$$\Delta f = \frac{K + 1}{2T}. \qquad [3]$$

Standard deviations of the power spectra are reported as jackknife estimates across all degrees of freedom (see ref. 19 for implementation).

The spectral coherence between pairs of time series, denoted $C(f)$ below, is defined analogously to the spectral power, with

$$\mathbf{C}(f) \equiv \frac{1}{NK} \sum_{n=1}^{N} \sum_{k=1}^{K} \tilde{\mathbf{V}}^{(n,k)} \tilde{\mathbf{U}}^{*(n,k)} / \sqrt{\mathbf{S}_{\mathrm{V}}(f)\mathbf{S}_{\mathrm{U}}(f)} \qquad \textbf{[4]}$$

where $\tilde{\mathbf{V}}^{(n,k)}$ and $\tilde{\mathbf{U}}^{(n,k)}$ are the Fourier transforms of the two respective time series. The spectral coherence is a complex-valued function of frequency, the magnitude of which is a normalized measure of the covariation between each of the spectral components of two time series and the phase of which, denoted $\Delta\phi$, corresponds to the difference between each spectral component in the two time series. The magnitude of the coherence will exceed

$$|\mathbf{C}| > \sqrt{1 - p^{(NK-1)^{-1}}} \qquad \textbf{[5]}$$

in $p \times 100\%$ of measurements (20). For a 95% confidence interval, which nominally corresponds to two standard deviations above chance, $p = 0.05$.

Experimental Results

We measured the LFP at 16 uniformly spaced locations along a radial axis throughout the entire depth of S1 cortex in anesthetized animals (Fig. 2*a*). In response to periodic taps to the vibrissae, the LFP is observed to exhibit a transient, multiphasic response; an example for taps at 6 Hz is shown in Fig. 2*b*. The calculation of the CSD, a measure of radial current flow into a region (17), removes common changes in potential and highlights temporal structure in current flow between layers (Fig. 2*c*).

Nature of the CSD. The stimulus-induced current flow is present in all layers and changes sign at the nominal boundary between layers 2/3 and 4, qualitatively consistent with results in past reports (21–23). The phase lag of the response relative to the stimulus varies as a function of depth and stimulus frequency and is greatest in the superficial layers (Fig. 2*d*), consistent with the integrative nature of input to these layers.

We consider the consistency of our CSD measurements with past measurements of the spike response in S1 cortex. First, Armstrong-James and Fox (24) showed that the spike count per vibrissa tap was proportional to the angular speed of the stimulus with a constant of proportionality that dropped in value for speeds above ≈250°/s; this is considerably slower than the speed of ≈2,000°/s observed during exploratory whisking (25). We observed that the initial slope of the CSD, a measure that minimizes polysynaptic contributions (26), was a monotonically increasing function of the angular speed of the tap that was qualitatively similar in form to that for spiking (Fig. 2*e*). Second, Ahissar *et al.* (10, 27) reported that the latency is independent of frequency at the level of layer 4, consistent with direct input from ventral posterior medial thalamus (28). A measure analogous to spike latency that is appropriate for continuous, periodic data is the time delay between the fundamental frequency of the CSD and the stimulus, defined by $\Delta\phi/2\pi f_s$. We observed that the delay was essentially independent of frequency for data obtained from depths corresponding to layer 4 (Fig. 2*f*) and deep layer 5 (not shown), consistent with past spike data. Last, Shuler *et al.* (29) showed that S1 cortex can be activated by ipsilateral as well as contraleral vibrissa stimulation. We observe that stimulation of the ipsilateral vibrissae leads to a measurable CSD response for stimulation frequencies up to 8 Hz; the peak-to-peak amplitude is 10 times less than that for contralateral stimulation (Fig. 2*g*). *In toto*, our CSD measurements are consistent with the average spike response in S1 cortex.

Mixing of Intrinsic and Evoked Rhythms. Ketamine-induced anesthesia leads to 1–6-Hz oscillations throughout cortex (30, 31). These oscillations varied in amplitude and frequency over periods of minutes, which were long compared with individual experimental epochs. By staging our stimulation during periods of strong oscillations, we could use these intrinsic oscillations as a means to generate an internal rhythm that serves as a surrogate for the reference signal in a sensory task.

We consider first an example with approximately $f_i \approx 1.8$-Hz oscillations in the absence of stimulation. These intrinsic oscillations are seen in the single trial time series throughout the CSD in almost all layers (Fig. 3*a Left*). After the application of an $f_s = 8.0$-Hz stimulus to the vibrissae, a strong rhythmic response is induced in the upper to middle layers of cortex (Fig. 3*a Left*). The spectral power density is used to quantify the response by effectively dissecting the measured CSD into individual frequency components. The spectral power exhibits peaks at the frequencies of the two fundamental oscillations as well as at harmonics of the stimulus frequency (Fig. 3*a Right*); the harmonics result from the pulsatile shape of the periodic taps to the vibrissae (7). Spectral peaks at the sum and difference of the two fundamental frequencies are visible most clearly in the middle to upper layers (Fig. 3*a Right*). The presence of the mixture frequencies only at subset of the depths for which the fundamental frequencies are present shows that spectral mixing is not a passive property of the extracellular space (e.g., 450 μm in Fig. 3*a Right*).

The trial-averaged spectra for the above example provides a means to estimate the significance of the response at different peaks. In the absence of stimulation to the vibrissae, we observed a single peak at the intrinsic frequency, $f_i \approx 1.8$ Hz (Fig. 3*b*, the solid line is the average spectrum, and the gray bands are the 95% confidence intervals). After stimulation of the vibrissa at a frequency of $f_s = 5.0$, 8.0, or 14.7 Hz, we observed statistically significant peaks in the spectrum at f_s as well as at the mixing frequencies $f_s \pm f_i$ (Fig. 3*b*). In a second example, the intrinsic oscillation was approximately $f_i = 5.5$ Hz, and we observed only the fundamental and its harmonics in the absence of stimulation. After stimulation of the vibrissa at a frequency of $f_s = 8$ Hz, we observed strong mixing with the intrinsic frequency (Fig. 3*c*).

We quantified the average power at the intrinsic frequency and at the mixture frequencies relative to that evoked by stimulation of the vibrissae. Our sample consisted of 65 epochs across 11 animals that showed 1.5- to 2.5-Hz intrinsic oscillations and 8 animals that showed strong 4- to 6-Hz oscillations. As an average across all epochs and animals and all layers in cortex, the ratio of the power at the intrinsic frequency to that induced by the external stimulus was 1.03 ± 0.17 (mean ± SEM). There was relatively little variation in this ratio when the responses were segregated according to superficial, upper, middle, and deep layers (Fig. 3*d*). Last, no significant difference was found in this ratio for the lower versus higher range of intrinsic frequencies. Thus, the power for the two fundamental terms, the intrinsic oscillation and the stimulus-induced oscillation, was statistically equivalent.

An analysis of the power at the two mixture frequencies, $f_s + f_i$ and $f_s - f_i$, was performed as an average across all epochs and animals and all layers in cortex similar to that described above. Here, the ratio of the power at the mixtures to that induced by the external stimulus was 0.12 ± 0.03 and 0.13 ± 0.03 for the $f_s + f_i$ and $f_s - f_i$ terms, respectively. The value of this ratio was slightly and significantly lower in the superficial layer as compared with other layers (Fig. 3*d*). Nonetheless, the average power at each of the two mixture terms was statistically equivalent, albeit much smaller than that for the intrinsic or stimulus-induced oscillation.

Mixing of Ipsilateral and Contralateral Evoked Rhythms. A second means to test for spectral mixing involved stimulation of both the contralateral and ipsilateral mystacial pads. We used pairs of different frequencies to simultaneously stimulate the mystacial pads

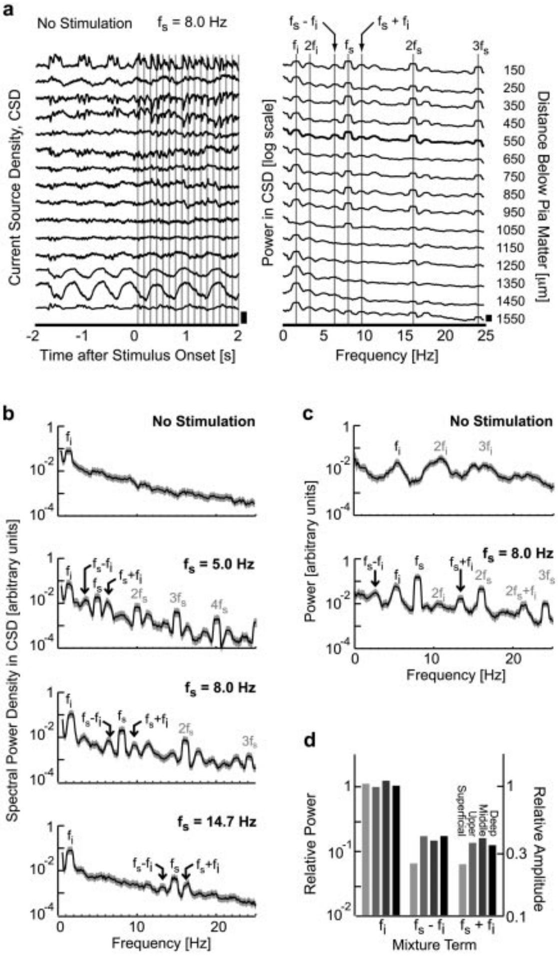

Fig. 3. Examples of spectral mixing between an intrinsic oscillation and a rhythmic sensory input. (*a Left*) A single epoch of the CSD time series as a function of depth below the pial surface. Note the presence of intrinsic rhythmic activity near 1.8 Hz in almost all layers, with a change in waveform between layers. The periodic stimulus starts halfway through the trace (gray bands) and is observed to modulate electrical activity most strongly in the upper layers. (Scale bar, 10 mV/mm^2.) (*a Right*) The spectral power density, averaged over $n = 10$, $T = 4.1$ s epochs of activity ($\Delta f = 0.5$ Hz with $K = 3$). Note the peaks at the intrinsic frequency, $f_i = 1.8$ Hz, and at its first harmonic $2f_i = 3.6$ Hz, the peaks at the stimulus frequency, $f_s = 8$ Hz, and at its harmonics, $2f_s = 16$ Hz and $3f_s = 24$ Hz, and the peaks at mixtures of these frequencies. The mixtures at $f_s - f_i = 6.2$ Hz and $f_s + f_i = 9.8$ Hz are most pronounced, whereas peaks at $f_s - 2f_i = 4.8$ Hz, $f_s + 2f_i = 11.6$ Hz, $2f_s - f_i = 14.2$ Hz, and $2f_s + f_i = 17.8$ Hz are observed also. The flattened top of some peaks results from averaging over Δf. (Scale bar, 1 decade.) (*b*) The spectral power density at a depth of 450 μm below the pial surface for different stimulation frequencies. Note the presence of the mixing terms $f_s \pm f_i$ except in the ''No Stimulation'' case and the presence of higher order mixing terms, i.e., $2f_s \pm f_i$, $3f_s \pm f_i$, and $4f_s \pm f_i$ in some instances. The gray bands correspond to 2 standard deviations, i.e., nominally the 95% confidence interval, around the mean value. (*c*) The spectral power density at a depth of 450 μm below the pia for a different animal ($\Delta f = 0.5$ Hz with $K = 3$, $T = 4.1$ s, and $n = 10$). Note the presence of peaks at the intrinsic frequency, $f_i = 5.5$ Hz, and at the harmonics $2f_i = 11$ Hz and $3f_i \approx 16$ Hz both before and during stimulation. Stimulation at $f_s = 8$ Hz leads to peaks at the stimulus frequency, $f_s = 8$ Hz, and at the harmonics $2f_s = 16$ Hz and $3f_s = 24$ Hz as well as strong peaks at the mixture frequencies $f_s - f_i = 2.5$ Hz and $f_s + f_i = 10.5$ Hz. The gray bands correspond to 2 standard deviations. (*d*) Summary of the relative power in the fundamental and mixture bands for all preparations ($n = 65$). We plot $\Sigma\mathbf{S}(f_i)/\Sigma\mathbf{S}(f_s)$, $\Sigma\mathbf{S}(f_s - f_i)/\Sigma\mathbf{S}(f_s)$, and $\Sigma\mathbf{S}(f_s + f_i)/\Sigma\mathbf{S}(f_s)$ for the superficial sink ($\approx$300 μm below the pia), upper sink, ($\approx$600 μm), middle sink ($\approx$1,000 μm), and deep layers ($\approx$1,300 μm).

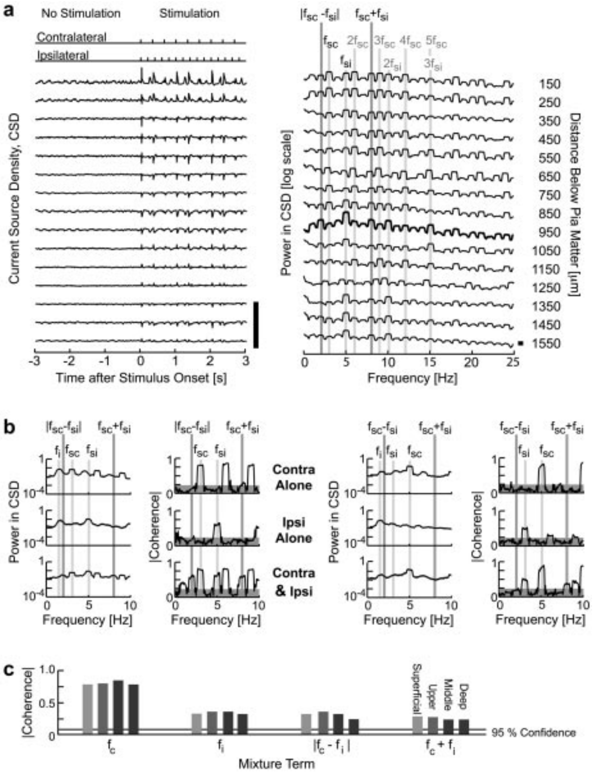

Fig. 4. Examples of spectral mixing between simultaneous stimulation to the ipsilateral and contralateral mystacial pads at different frequencies. (*a Left*) The time series of the CSD as a function of depth below the pial surface. The data are the stimulus-locked average of 10 consecutive trials. The periodic stimuli start halfway through the trace, as indicated on the two lines on top, and is observed to modulate electrical activity most strongly in the upper and middle layers. Note that some intrinsic rhythmic activity is present before stimulation. (Scale bar, 100 mV/mm^2.) (*Right*) The spectral power density, averaged over $n = 10$, $T = 8.2$ s epochs of activity ($\Delta f = 0.4$ Hz with $K = 5$). Note the peaks at the contralateral stimulus frequency, $f_{sc} = 3.0$ Hz, and at its harmonics, $2f_{sc} = 6.0$ Hz through $8f_{sc} = 24.0$ Hz, the peaks at the ipsilateral stimulus frequency, $f_{si} = 5.0$ Hz, and at its harmonics, $2f_{si} = 10.0$ Hz through $4f_{sc} = 20.0$ Hz, and the peaks at mixtures of these frequencies, $|f_{sc} - f_i| = 3.0$ Hz and $f_s + f_i = 8.0$ Hz. Peaks at additional mixture frequencies, including $2f_{sc} - f_{si} = 1.0$ Hz, are observed also. (Scale bar, 1 decade.) (*b*) The spectral power and the spectral coherence between the CSD and sine waves at all harmonic and mixture frequencies that were synthesized from the stimuli. ($T = 8.2$ s with $\Delta f = 0.4$ Hz and $K = 5$.) (*Top*) The response with only the contralateral stimulus present. (*Middle*) The response with only the ipsilateral stimulus present. (*Bottom*) The response with both stimuli present. The gray bands in the coherence plot denote the 95% confidence interval. The data were obtained at a depth of 650 μm below the pia. The right and left set of columns refer to an interchange of the contralateral (contra) and ipsilateral (ipsi) stimulation frequencies. (*c*) Summary of the relative coherence in the fundamental and mixture bands for all preparations.

on both sides of the head during periods for which the ketamine-induced oscillations were relatively weak. An example for the case of contralateral stimulation at $f_{sc} = 3$ Hz and ipsilateral stimulation at $f_{si} = 5$ Hz is shown in Fig. 4*a*. The spectral power shows significant peaks at the stimulus frequencies and at harmonics of those frequencies, as well as peaks at the mixture frequencies $f_{sc} \pm f_{si}$, throughout much of the depth of cortex.

As a result of the relatively weak response to ipsilateral stimulation (Fig. 2*g*) and ongoing intrinsic electrical activity, estimates of the spectral power were often insufficiently sensitive to report stimulation of the ipsilateral vibrissae (Fig. 4*b*) and thus could fail to detect cortical activity at the mixture frequencies. Increased sensitivity to spectral components that were phase-locked to the stimuli was achieved by calculating the spectral coherence between the CSD signal and all possible harmonic and mixture frequencies. For example, contralateral stimulation at $f_{sc} = 3$ Hz led to peaks solely at this frequency and its harmonics, ipsilateral stimulation at $f_{si} = 5$ Hz led to peaks solely at this higher frequency and its harmonics, whereas simultaneous stimulation at both frequencies led to the additional presence of mixture terms at $f_{sc} \pm f_{si}$ (left columns in Fig. 4*b*). This effect persisted, albeit with weaker mixing terms in this example, when the contralateral and ipsilateral stimuli were interchanged (left columns in Fig. 4*b*), as well as when the initial phase between the two frequencies was varied (data not shown). A summary across all epochs and animals and all layers in cortex ($n = 6$ animals with 60 trials using all pairwise permutations of 3-, 5-, and 8-Hz vibrissa stimulation) shows that the coherence is greatest for contralateral stimulation and that it is significant, at the 95% confidence level, across all lamina at both the stimulation frequencies as well as at the mixture frequencies. There was insignificant variation in the coherence when the responses were segregated according to superficial, upper, middle, and deep layers (Fig. 4*c*).

Theory

Spectral mixing can be generated by any nonlinear process such as the multiplication of signals. There is support for multiplication at the level of receptive field formation, e.g., neurons code the confluence of gaze direction and retinal location in vision (32, 33) and the outer product of azimuth versus elevation source-coding in audition (34), and as an element in motion detection (35) and depth detection (36) in vision. However, a purely multiplicative process cannot explain the presence of strong peaks at the fundamental frequencies as well as the mixture frequencies in the CSD data (Figs. 3 and 4), nor, as a matter of principle, can it explain peaks at mixtures other than the sum and difference of the fundamental frequencies. As a means to explore whether mixing can be achieved with a minimalist model of neuronal behavior, we considered the effect of a threshold input–output relation on the summation of two sinusoidal signals. Such relations lead to other emergent phenomena, such as multistability, at the systems level (37, 38).

Threshold Model. We take the input to the cell as $x(t) = \cos(2\pi f_a t) + \rho\cos(2\pi f_b t)$, with $0 < \rho \leq 1$ and define the output as $H[x(t) - \theta_o]$, where $H(x)$ is the Heavyside function and θ_o is the value of the threshold, i.e., $H(x - \theta_o) = 0$ for $x < \theta_o$ and $H(x - \theta_o) = 1$ for $x \geq \theta_o$. The spectral power of the output can be expressed in terms of closed integrals (see *Appendix*). It has contributions at all possible mixture frequencies, i.e., for $|mf_a \pm nf_b|$, where n and m are integers, although the low-order mixing terms will have the greatest amplitude. The general dependence of the power at the fundamental frequencies, f_a and f_b, and at the lowest-order mixing frequencies, $f_a \pm f_b$, is shown in Fig. 5 *a*–*c* as a function of ρ and θ_o. The power in the mixture modes is maximized along the lines $\rho = 1.0$ and achieves an absolute maximum for $\theta_o = 0.8$ (Fig. 5*c*). In the limit that only the lowest-order mixing terms significantly contribute to the spectrum, as suggested by the data (Fig. 3 *b* and *c*), the symmetry of this model implies that the power is the same for the sum and difference frequencies (see *Appendix*). In this limit, the power in mixture modes relative to that in the fundamental f_a can be calculated and compared with the observation (Fig. 3*d*); we find that $\rho = 1.0$ and $\theta_o = 0.3$ are consistent with the trial-averaged response (Fig. 5*d*, ●).

As a specific example of the behavior of the threshold model, the input and output are illustrated for the case of $f_a = 5$ Hz, $f_b = 8$ Hz, $\rho = 1.0$, and $\theta_o = 0.8$ (Fig. 5 *e* and *f*). The spectrum of the output is discrete in multiples of the maximum divisor of f_a and f_b, i.e., 1 Hz for this case. For our choice of θ_o, the spectrum exhibits peaks at the fundamental and mixing frequencies, the relative amplitudes of which are in qualitative agreement with the particular example of Fig. 3*c*.

Hindmarch–Rose Model. As a check to determine whether spectral mixing is generated by more realistic models of neuronal dynamics, we considered the output from a Hindmarch–Rose model (39). This model is described by three ordinary differential equations (see *Appendix*) and exhibits oscillatory bursts of spikes and chaotic behavior as well as periodic spiking (40). We chose parameters that lead to periodic spiking with a constant input current, i.e., $\mathbf{I} = \mathbf{I}_o$, and observed that the addition of two small oscillatory currents, at $f_a = 5$ Hz and $f_b = 8$ Hz as described above, lead to robust mixture terms in the spectral power of the output (Fig. 5 *h* and *i*). The power at the difference term, $f_b - f_a$, is larger than that at the summation term as a consequence of low-pass filtering by the model neuron.

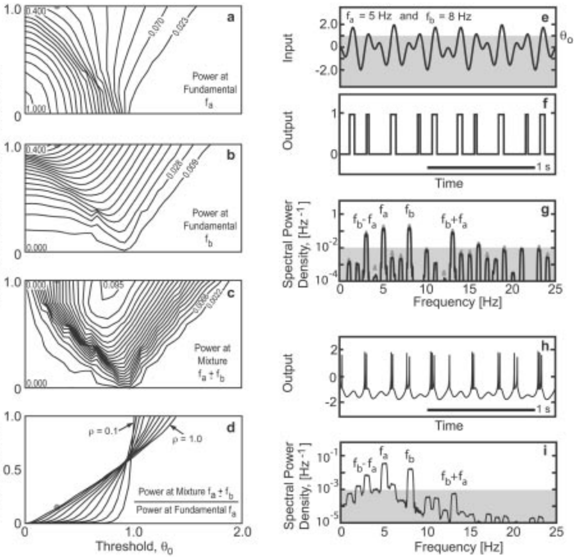

Fig. 5. Properties of the threshold model for spectral mixing. (*a*–*c*) Numerical evaluation of the power for the threshold model $H[\cos(2\pi f_a t) + \rho\cos(2\pi f_b t) - \theta_0]$ at the fundamental frequencies f_a and f_b and at the mixing frequencies $f_a \pm f_b$. The contour plots were derived from numerical evaluation of the individual terms $|I_{1,0}(\theta_0,\rho)|^2/4$, $|I_{0,1}(\theta_0,\rho)|^2/4$, and $|I_{1,\,1}(\theta_0,\rho)|^2/4$, respectively, and drawn with contour steps of 0.0465, 0.0186, and 0.0044. The numbers in the left-hand corners refer to specific values of the power for $\rho = 0$ or 1.0. (*d*) Numerical evaluation of the power at the mixture modes over that at the fundamental mode; we plot $|I_{1,1}(\theta_0,\rho)|^2/|I_{1,0}(\theta_0,\rho)|^2$ for selected values of ρ. The gray circle refers to the parameters that best fit the experimental observations. (*e*–*g*) Example of the threshold model for the choice $\rho = 1.0$, $f_a = 5$ Hz, and $f_b = 8$ Hz, where the threshold was taken to have a value of $\theta_0 = 0.8$ (gray band in *e*). The spectral density for this output was computed in two ways. First (filled triangles), the spectrum was calculated by direct evaluation of the transform of the output subsequent to the determination of the onset and offset time of each interval, i.e., the solutions of $\cos(2\pi f_a t) + \cos(2\pi f_b t) - \theta_0 = 0$ over the 1-s period of one repetition (*e*). Second (solid lines), the spectrum was computed from a 10-s time series (*f*) by using $\Delta f = 0.2$ Hz. The gray band is drawn at the height of the noise floor for the data, i.e., an ≈1 decade with a signal-to-noise ratio greater than 1 (Fig. 3). (*h* and *i*) Example of the Hindmarsh–Rose model for the choice $f_a = 5$ Hz, $f_b = 8$ Hz, $\Delta_a = 0.15$, and $\Delta_b = 0.05$. *h* shows the fast variable, $x(t)$. The spectrum in *i* was calculated with a bandwidth of $\Delta f = 0.35$ Hz.

Conclusion

Our data provide support for spectral mixing (Fig. 1) as a component of sensory coding in the rat vibrissa system (Figs. 3 and 4). Mixing is an essential element of schemes to deduce the frequency or phase difference between two signals (Fig. 1). It may be used to compute the position of vibrissa contact in head-centered coordinates and as part of a circuit to lock internal oscillators to an external rhythmic input. We further suggest that other neuronal functions that involve rhythmic sensory and motor signals may rely on mixing as an essential computational element. Most notable is the detection of auditory beats from binaural inputs (2).

Our data do not address the anatomical substrate for mixing. Nonetheless, the results of our modeling efforts imply that the threshold behavior of neurons is sufficient to explain the observed mixing (Fig. 5). The simplicity of this mechanism suggests that spectral mixing may be a ubiquitous component of computing with oscillatory neuronal signals.

Appendix

Threshold Model. We evaluate the spectral power for an output that consists of a threshold, or step function, applied to a sinusoidal input, $x(t) = \cos(\omega_a t) + \rho\cos(\omega_b t)$, where $\omega = 2\pi f$. Recall that the step function, denoted $H[x - \theta_0]$, where θ_0 is the threshold, can be expressed as an inverse Laplace transform. Thus

$$\begin{aligned} &H[\cos(\omega_a t) + \rho\cos(\omega_b t) - \theta_0] \\ &\quad = \frac{1}{2\pi i}\int_{\varepsilon - i\infty}^{\varepsilon + i\infty} \frac{ds}{s} e^{s[\cos(\omega_a t) + \rho\cos(\omega_b t) - \theta_0]} \\ &\quad = \frac{1}{2\pi i}\int_{-\infty}^{+\infty} \frac{d\Omega}{\Omega - i\varepsilon} e^{i\Omega[\cos(\omega_a t) + \rho\cos(\omega_b t) - \theta_0]}, \end{aligned} \qquad [6]$$

where the contour runs along the real axis in the latter integral, and $\varepsilon \rightarrow 0$. We further recall the expansion

$$e^{i\Omega\cos\phi} = \sum_{k=-\infty}^{+\infty} J_k(\Omega) i^k e^{ik\phi}, \qquad [7]$$

where $J_k(\Omega)$ is the Bessel function of order k such that

$$\begin{aligned} &H[\cos(\omega_a t) + \rho\cos(\omega_b t) - \theta_0] \\ &\quad = \frac{1}{2\pi i} \sum_{n=-\infty}^{\infty} \sum_{m=-\infty}^{\infty} e^{i\frac{\pi}{2}(n+m)} e^{i(n\omega_a + m\omega_b)t} \cdot \mathbf{I}_{nm}(\theta_0, \rho). \end{aligned} \qquad [8]$$

Spectral mixing results from the argument of the exponential terms. The integral

$$\mathbf{I}_{nm}(\theta_0, \rho) \equiv \int_{-\infty}^{+\infty} \frac{d\Omega}{\Omega - i\varepsilon} e^{-i\theta_0\Omega} J_n(\Omega) J_m(\rho\Omega) \qquad [9]$$

sets the magnitude for each term and, in general, must be evaluated numerically. Recall that $J_k(\Omega) = (-1)^k J_{-k}(\Omega)$ so that $\mathbf{I}_{-n,m}(\theta_0, \rho) = (-1)^n\, \mathbf{I}_{n,m}(\theta_0, \rho)$, etc., and sum and difference terms of the same order have equal magnitudes.

The spectral representation for the output of the model is denoted by $\tilde{G}(\omega)$, where

$$\begin{aligned} \tilde{G}(\omega) &\equiv \int_{-\infty}^{+\infty} dt e^{-i\omega t} H[x(t) - \theta_0] \\ &= -i \sum_{n=-\infty}^{\infty} \sum_{m=-\infty}^{\infty} e^{i\frac{\pi}{2}(n+m)} \delta[\omega - (n\omega_a + m\omega_b)] \cdot \mathbf{I}_{nm}(\theta_0, \rho), \end{aligned} \qquad [10]$$

and we used the identity

$$\delta(\Omega) = \frac{1}{2\pi}\int_{-\infty}^{+\infty} dt e^{-i\Omega t}. \qquad [11]$$

The addition of arbitrary phase shifts to the input sinusoids, such that $\omega_a t \leftarrow \omega_a t + \psi_a$ and $\omega_b t \leftarrow \omega_b t + \psi_b$, changes the spectral representation to read

$$\begin{aligned} \tilde{G}(\omega) = -i \sum_{n=-\infty}^{\infty} \sum_{m=-\infty}^{\infty} & e^{i[n(\psi_a + \pi/2) + m(\psi_b + \pi/2)]} \\ & \delta[\omega - (n\omega_a + m\omega_b)] \cdot \mathbf{I}_{nm}(\theta_0, \rho), \end{aligned} \qquad [12]$$

but does not change the magnitude of a given term in the summation. Last, the power for a particular (n, m)th term alone is $|\mathbf{I}_{nm}(\theta_0, \rho)|^2$, where $(n, m) = (1,0)$ and $(-1,0)$ for the fundamental at ω_a, $(0,1)$ and $(0,-1)$ for the fundamental at ω_b, $(1,1)$ and $(-1,-1)$ for the sum frequency, and $(1,-1)$, and $(-1,1)$ for the difference frequency.

Review of Hindmarch–Rose Model. This is a system of three ordinary differential equations that is described by the variables x, a fast variable that tracks voltage, y, a variable that tracks recovery, and z, a variable that tracks adaptation (40). The dynamics are given by $dx/\mathrm{dt} = -Ax^3 + Bx^2 + y - z + \mathbf{I}$, $dy/dt = -\mathrm{C}x^2 - y + D$, and $dz/dt = E(x - x_0) - Fz$ with parameters $A = 1.0$, $B = 3.0$, $C = 5.0$, $D = 1.0$, $E = 0.024$, $F = 0.006$, and $x_0 = -1.6$. The current was $\mathbf{I} = \mathbf{I}_0[1 + \Delta_a\cos(2\pi f_a t) + \Delta_b\cos(2\pi f_b t)]$ with $\mathbf{I}_0 = 1.5$.

We thank David J. Andersen and Jamille F. Hetke of the Center for Neural Communication Technology for supplying the multisite probes; Ehud Ahissar, Jean-Marc Fellous, Beth Friedman, Karunesh Ganguly, Eugene Izhikevich, and Terrence Sejnowski for comments on early versions of the manuscript; Shannon Hefler for assistance with the histology; Harvey Karten for use of his photomicroscope; Ford F. Ebner, William Kristan, Jr., and H. Sebastian Seung for informative discussions; and G. Allen White for assistance with the electronics. This work was supported by a National Research Service Award fellowship (to K.F.A.) and National Institutes of Health Grant MH59867 (to D.K.).

1. Licklider, J. C. R., Webster, J. C. & Hedlon, J. M. (1950) *J. Acoust. Soc. Am.* **22,** 468–473.
2. Oster, G. (1973) *Sci. Am.* **229,** 94–102.
3. Bullock, T. H. & Heiligenberg, W. (1987) *Electroreception* (Wiley, New York).
4. Suga, N. (1989) *Exp. Biol.* **46,** 277–286.
5. Fee, M. S., Mitra, P. P. & Kleinfeld, D. (1997) *J. Neurophysiol.* **78,** 1144–1149.
6. Kleinfeld, D., Berg, R. W. & O'Connor, S. M. (1999) *Somat. Motil. Res.* **16,** 69–88.
7. Kleinfeld, D., Sachdev, R. N. S., Merchant, L. M., Jarvis, M. R. & Ebner, F. F. (2002) *Neuron* **34,** 1021–1034.
8. Ahissar, E. & Vaadia, E. (1990) *Proc. Natl. Acad. Sci. USA* **87,** 8935–8939.
9. Ahissar, E. (1998) *Neural Comput.* **10,** 597–650.
10. Ahissar, E., Haidarliu, S. & Zackenhouse, M. (1997) *Proc. Natl. Acad. Sci. USA* **94,** 11633–11638.
11. Best, R. E. (1984) *Phase-Locked Loops: Theory, Design, and Applications* (McGraw–Hill, New York).
12. National Institutes of Health (1985) *Guide for the Care and Use of Laboratory Animals* (Natl. Inst. Health, Bethesda), NIH Publ. No. 85-23.
13. Kleinfeld, D. & Delaney, K. R. (1996) *J. Comp. Neurol.* **375,** 89–108.
14. Simons, D. J. (1983) *Brain Res.* **276,** 178–182.
15. Jones, M. S. & Barth, D. S. (1999) *J. Neurophysiol.* **82,** 1599–1609.
16. Prechtl, J. C., Bullock, T. H. & Kleinfeld, D. (2000) *Proc. Natl. Acad. Sci. USA* **97,** 877–882.
17. Nicholson, C. & Freeman, J. A. (1975) *J. Neurophysiol.* **38,** 356–368.
18. Thomson, D. J. (1982) *Proc. IEEE* **70,** 1055–1096.
19. Percival, D. B. & Walden, A. T. (1993) *Spectral Analysis for Physical Applications* (Cambridge Univ. Press, Cambridge, U.K.).
20. Jarvis, M. R. & Mitra, P. P. (2001) *Neural Comput.* **13,** 717–749.
21. Di, S., Baumgartner, C. & Barth, D. S. (1990) *J. Neurophysiol.* **63,** 832–840.
22. Schroeder, C. E., Lindsley, R. W., Specht, C., Marcovici, J. F., Smiley, J. F. & Javitt, D. C. (2001) *J. Neurophysiol.* **85,** 1322–1327.
23. Kulics, A. T. & Cauller, L. J. (1986) *Exp. Brain Res.* **62,** 46–60.
24. Armstrong-James, M. & Fox, K. (1987) *J. Comp. Neurol.* **263,** 265–281.
25. Gao, P., Bermejo, R. & Zeigler, H. P. (2001) *J. Neurosci.* **21,** 5374–5380.
26. Lomo, T. (1971) *Exp. Brain Res.* **12,** 18–45.
27. Ahissar, E., Sosnik, R., Bagdasarian, K. & Haidarliu, S. (2001) *J. Neurophysiol.* **86,** 454–467.
28. Hartings, J. A. & Simons, D. J. (1998) *J. Neurophysiol.* **80,** 1016–1019.
29. Shuler, M. G., Krupa, D. J. & Nicolelis, M. A. (2001) *J. Neurosci.* **21,** 5251–5261.
30. Volgyesi, G. A. (1978) *Can. Anaesth. Soc. J.* **25,** 427–430.
31. Soltesz, I., Bourassa, J. & Deschenes, M. (1993) *Neuroscience* **57,** 555–564.
32. Salinas, E. & Abbott, L. F. (1996) *Proc. Natl. Acad. Sci. USA* **93,** 11956–11961.
33. Andersen, R. A. & Mountcastle, V. B. (1983) *J. Neurosci.* **3,** 532–548.
34. Pena, J. L. & Konishi, M. (2001) *Science* **292,** 249–252.
35. Egelhaaf, M., Borst, A. & Reichardt, W. (1989) *J. Opt. Soc. Am. A* **6,** 1070–1087.
36. Anzai, A., Ohzawa, I. & Freeman, R. D. (1999) *J. Neurophysiol.* **82,** 891–908.
37. Hopfield, J. J. (1982) *Proc. Natl. Acad. Sci. USA* **79,** 2554–2558.
38. Ben-Yishai, R., Lev Bar-Or, R. & Sompolinsky, H. (1995) *Proc. Natl. Acad. Sci. USA* **92,** 3844–3848.
39. Hindmarch, J. L. & Rose, R. M. (1984) *Proc. R. Soc. London Ser. B* **221,** 87–102.
40. Kaas-Petersen, C. (1986) in *Chaos in Biological Systems*, eds. Degn, H., Holden, A. V. & Olsen, L. F. (Plenum, New York), pp. 183–190.